Recibido: 01/05/2020
Aceptado: 06/04/2021

REVISTA DE TELEDETECCIÓN
Asociación Española de Teledetección
(2021) 58, 39-52
ISSN 1133-0953
EISSN 1988-8740
https://doi.org/10.4995/raet.2021.13622

Mapping Sandy Areas and their changes using remote sensing. A Case Study at North-East Al-Muthanna Province, South of Iraq

Awad A. Sahar*[1], Muaid J. Rasheed[2], Dhia A. A.-H. Uaid[3], Ammar A. Jasim[4]

[1]*Department of surveying techniques, Middle Technical University, Al-Kut, Iraq.*
[2]*Department of Earth science, Baghdad University, Baghdad, Iraq.*
[3]*Department of Geography, College of Education for Human Sciences, Wasit University, Al-Kut, Iraq.*
[4]*Remote Sensing Center, Ministry of Science and Technology, Baghdad, Iraq.*

Abstract: Sandy areas are the main problem in regions of arid and semi-arid climate in the world that threaten urban life, buildings, agricultural, and even human health. Remote sensing is one of the technologies that can be used as an effective tool in dynamic features study of sandy areas and sand accumulations. In this study, two new indices were developed to separate the sandy areas from the non-sandy areas. The first one is called the Normalized Differential Sandy Areas Index (NDSAI) that has been based on the assumption that the sandy area has the lowest water content (moisture) than the other land cover classes. The second other is called the Sandy Areas Surface Temperature index (SASTI) which was built on the assumption that the surface temperature of sandy soil is the highest. The results of proposed indices have been compared with two indices that were previously proposed by other researchers, namely the Normalized Differential Sand Dune Index NDSI and the Eolain Mapping Index (EMI). The accuracy assessment of the sandy indices showed that the NDSAI provides very good performance with an overall accuracy of 89 %. The SASTI can isolate many sandy and non-sandy pixels with an overall accuracy about 86 %. The performance of the NDSI is low with an overall accuracy about 82 %. It fails to classify or isolate the vegetation area from the sandy area and might have better performance in desert environments. The performing of NDSAI that is calculated with the SWIR1 band of the Landsat satellite is better than the performing of NDSI that is calculated with the SWIR2 band of the same satellite. EMI performance is less robust than other methods as it is not useful for extracting sandy surfaces in area with different land covers. Change detection techniques were used by comparing the areas of the sandy lands for the periods from 1987 to 2017. The results showed an increase in sandy areas over four decades. The percentage of this increase was about 20 % to 30 % during 2002 and 2017 compared to 1987.

Key words: remote sensing, sand dunes, Eolin mapping index, Landsat images, NDSAI.

Cartografiado de áreas arenosas y sus cambios mediante teledetección. Caso de estudio en el noreste de la provincia de Al-Muthanna, sur de Irak

Resumen: Las áreas arenosas son el principal problema en las regiones de clima árido y semiárido del mundo que amenazan la vida urbana, los edificios, la agricultura e incluso la salud humana. La teledetección es una de

To cite this article: Sahar, A.A., Rasheed, M.J., Uaid, D.A.A.H., Jasim, A.A. 2021. Mapping Sandy Areas and their changes using remote sensing. A Case Study at North-East Al-Muthanna Province, South of Iraq. *Revista de Teledetección*, *58*, 39-52. https://doi.org/10.4995/raet.2021.13622

* *Corresponding author: asmhy60@gmail.com*

Attribution-NonCommercial-ShareAlike 4.0 International (CC BY-NC-SA 4.0)

las tecnologías que puede utilizarse como una herramienta eficaz en el estudio de características dinámicas de áreas arenosas y acumulaciones de arena. En este estudio, se desarrollaron dos nuevos índices para separar las áreas arenosas de las áreas no arenosas. El primero llamado Índice de áreas arenosas diferenciales normalizadas (NDSAI), que se ha basado en el supuesto de que el área arenosa tiene el contenido de agua (humedad) más bajo que las otras clases de cobertura del suelo. El segundo llamado índice de temperatura superficial de las áreas arenosas (SASTI), que se basa en el supuesto de que la temperatura superficial del suelo arenoso es la más alta. Estos nuevos índices se han comparado con dos índices propuestos previamente por otros investigadores, a saber, el Índice de dunas de arena diferencial normalizado NDSI y el Eolain Mapping Index (EMI). La evaluación de la precisión de los índices arenosos mostró que el índice NDSAI proporciona un buen desempeño con una precisión general del 89 %. El índice SASTI puede extraer muchos píxeles arenosos y no arenosos con una precisión general del 86 %. El rendimiento del índice NDSI es pobre, con una precisión general del 82 %, no puede clasificar o aislar el área de vegetación del área arenosa y tal vez funcione mejor en entornos desérticos. El índice NDSAI calculado con la banda SWIR1 del satélite Landsat generó resultados más precisos que el NDSI calculado con la banda SWIR2 del mismo satélite. El índice EMI utilizado fue menos robusto que los otros métodos ya que no ha logrado extraer áreas arenosas con una precisión aceptable en áreas con diversas coberturas terrestres. Se utilizaron técnicas de detección de cambios para analizar las áreas de las tierras arenosas para los períodos de 1987 a 2017. Los resultados marcaron un aumento en las áreas arenosas durante cuatro décadas. El porcentaje de este aumento fue de aproximadamente 20 % a 30 % durante 2002 y 2017 en comparación con 1987.

Palabras clave: teledetección, dunas de arena, índice de mapeo Eolin, imágenes Landsat, NDSAI.

1. Introduction

Sandy areas occur throughout the world and spread in all continents and all different world climates (Hillel and Hatfield, 2005), and they are the main problem in arid and semi-arid regions that sometimes threaten urban and buildings cities, agricultural farms and human health (Walker, 2009). A sandy area is a land degradation feature which may thus lead to desertification (Bagnold, 2012). There are about 20% of the arid and the extreme arid regions around the world covered with sand dunes with an area of more than 5 million km^2, 99% of them are desert areas (Hillel and Hatfield, 2005). There is about 10% of the Earth's surface between latitudes 30° north and south covered by sandy areas (Levin and Ben-Dor, 2004). Sandy phenomena can develop into different shapes and sizes depending on the factors that have formed them, for example, the variation in the wind direction, vegetation cover, and grain size (Pye and Tsoar, 2008).

Sandy areas represent a danger to agricultural economic projects, roads, and various other human activities. More than 93 percent of Iraqi lands are affected by soil erosion (Fadhil, 2013), especially in central and southern Iraq. The northeast part of the Al-Muthanna province suffers from an accelerated movement of sand dunes of varying sizes and shapes.

Remote sensing (RS) is one of the rapidly growing technologies that can supply reliable and low-cost information for changes in environmental conditions and at local, regional and global levels (Lee et al., 2018). The images of RS were first used in the study of sandy lands and patterns of sand dunes in the early 1970s (Hugenholtz et al., 2012). Previous studies utilized Landsat (ERTS) imagery to describe the extensive dunes patterns for the largest sandy areas in the world (Breed et al., 1979a; 1979b). McKee (1979) focused on the mapping sandy terrain and categorizing dune types, which were mainly associated with control of variables such a sand supply and changing wind direction (Wasson and Hyde, 1983). In the 1980s, studies were focused on studying individual dunes (Azzaoui et al., 2019). Developments in hardware and software of computers during the 1990s simplified the study of the reflectance properties of sand dune surfaces (Paisley et al., 1991; Pease et al., 1999; Tsoar and Karnieli, 1996). Consequently, new methods for identifying changes in sand dune activity were found (Brown and Arbogast, 1999). The enhancements in the spatial and spectral resolution of the RS images (such as the US Landsat8 satellite that launched on

February 11, 2013, and the European Sentinel2 A & B satellites, which launched on June 23, 2015, and March 7, 2017, respectively) have greatly enhanced the researcher's ability to solve dune processes and features (Wolfe and Hugenholtz, 2009). The RS indices such as vegetation indices, water indices, and build-up indices are widely utilized for estimating different types of land cover such as vegetation cover, water cover, and built-up cover, etc. (Rouse et al., 1974; Gao, 1996; Zha et al., 2003). The spectral reflectance or spectral signatures for sand landscapes such as sand sheet, sandy dunes, coastal regions, and inland areas are influenced by many factors, the most important of which are the morphological features, sand grains shape and size (Baranoski et al., 2013), and moisture content of their constituent grains (Kourdian, 2009).

Extraction of sandy areas and monitor their changes can be done defining the spectral signature. The first index used to evaluate sand dunes was the NDSI (Normalized Differential Sand Index) developed by Fadhil (2009) based on the normalized difference of the spectral values between the RED and the SWIR2 bands of the Landsat5 satellite (TM sensor). The NDSI aimed to highlight and identify the presence of drifting sands and accumulations of sand dunes. The main NDSI limitation is the misclassification of non-sandy pixels especially the vegetation areas, and mixed pixels. The equation of NDSI is (Fadhil, 2009):

$$NDSI = \frac{R - SWIR2}{R + SWIR2} \quad (1)$$

Where R represents the reflectance of red band of the Landsat TM sensor (0.63–0.69 μm); SWIR-2 represents the reflectance of a short wavelength infrared band (2.08–2.35 μm). The NDSI values ($-1 \leq NDSI \leq 1$). Drifting sands and sand dunes accumulations have values less than zero (<0).

Eolation process or wind erosion is a natural risk in arid regions since it destroys soil sources and makes facial morphological changes (Yamani and Karami, 2011). Eolain Mapping Index (EMI) was proposed by (Khiry, 2007); it is a simple model created to produce an image that highlights areas with high soil reflectivity and low vegetation density. The EMI is based on the use of spectral compensation of near-infrared (NIR), red (Red), and the ratio of the red band to near-infrared (R/NIR) band of the Landsat sensors (MSS, TM, and ETM) to create an image that emphasizes lands with low/no vegetative cover and/or lands with high surface-soil reflectance (Abbas, 2010). The EMI has many limitations in extracting sandy surfaces in a region with different land covers.

The thermal infrared (TIR) region (8–12 μm) can be used to identify and mapping sandy land more accurately due to its emitted energy nature (linear nature). Sandy land, therefore, provides an excellent target for testing linear algorithms because it generally lacks thermal shadows and is composed of large particles. Moreover, the major dune forming minerals (such as sulfates, silicates, and carbonates) have characteristic absorption features in the thermal region (8–12 μm), which helps to make the detection of dunes easier (Ramsey et al., 1999).

The main objectives of this work are: (i) using RS data (optical and thermal of Landsat images) to develop new indices to estimate sandy areas; (ii) comparing the results of new sandy indices with other such as NDSI and EMI (iii) to determining the best and more accurate index to estimate sandy area.

2. Research Area

The study area is part of Al-Muthanna province, south of Iraq, within the Mesopotamian Zone. It covers about 5454 km^2 with about 68.1 km long and an average of 80 km wide; the elevation of this area ranges from 2 m to 96 m (Figure 1).

The study area belongs to the Mesopotamian region which is one of the main structural zones in Iraq. This zone is subjected to the great subsidence in the Mesozoic time through the slight folding of sedimentary covers culminating in the late Cenozoic (Buday, 1980).

The geological map of Al - Nasiriya of the Iraqi Geological Survey (Figure 2) was used to indicate the geology of the studied area. The stratigraphic units of the study area lie within Salman Zone and Mesopotamian Zone. About one-third of the Iraq surface is covered with quaternary sediments (Jassim and Goff, 2006), mostly within the Mesopotamian plain, and were comprised of marsh sediments, flood plain sediments, eolian sediments, and shallow depression sediments.

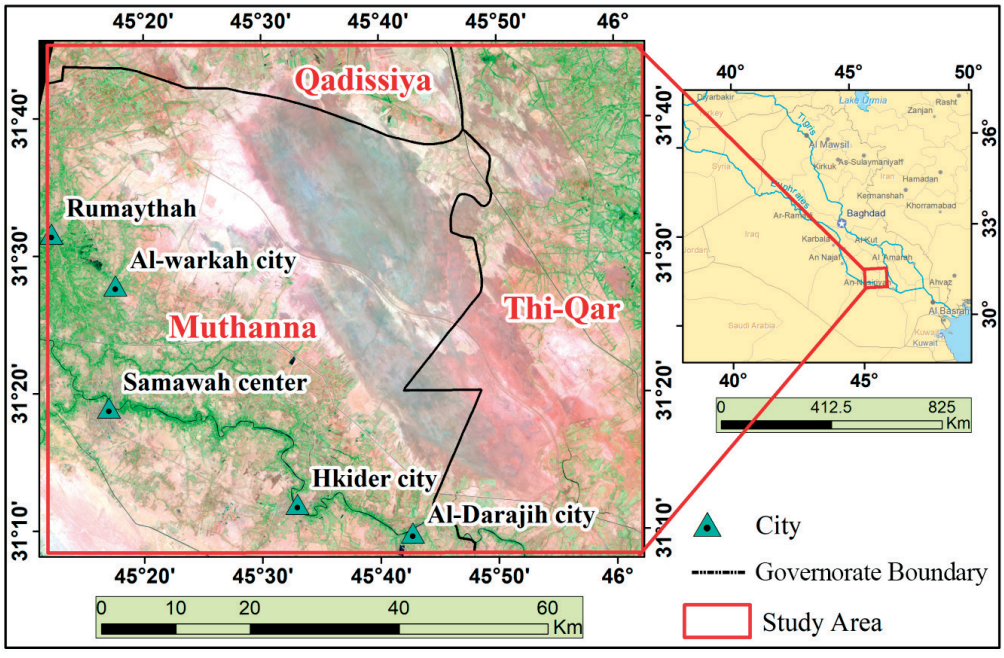

Figure 1. Location map of the study area, the image is Landsat8 6.4.2 RGB taken on 15/July/2017.

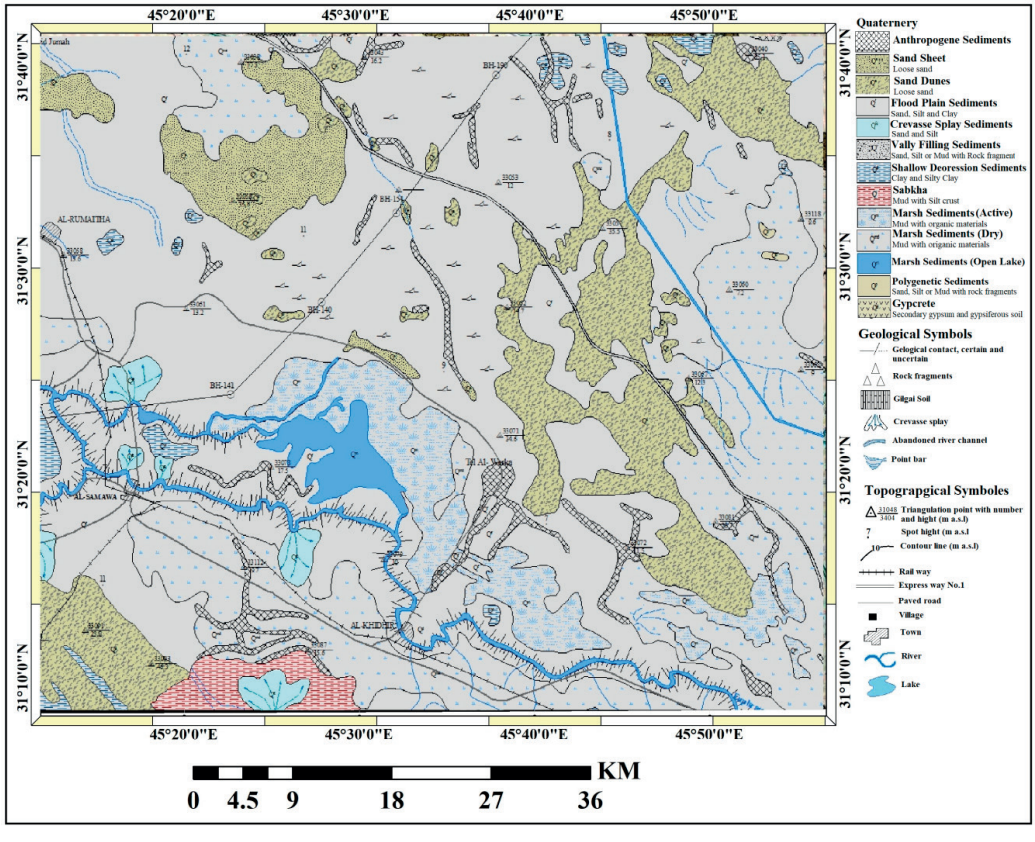

Figure 2. Geological map of the study area (Iraqi Geological survey and mining).

The climate of the research area is mostly arid (long, dry, hot summers, and short, rainy, cold winters) with the prevalence of desert conditions (Abdul-Ameer, 2012). According to Al-Samawa station (N 31.30°, E 45.26°) and Iraqi meteorological organization, the average annual rainfall is 95.29 mm per year, while the mean annual temperature is greater than 24 °C. The wind direction is primarily from the northwest (NW) and west (W) with an average annual speed of 3.15 m/s (State Company for Geological Survey and mining, 2012).

3. Materials and preprocessing

3.1. Materials

Cloud-free Thematic Mapper (TM) Landsat-5, Enhanced Thematic Mapper (ETM) Landsat-7, and Operational Land Imager OLI Landsat-8 images for level-1 (raw data) and level-2 (Surface Reflectance data products) were downloaded from US Geological Survey website (https://earthexplorer.usgs.gov/). The Landsat images (level-1) were used to estimate land surface temperature (LST) by utilizing thermal bands, while the Landsat images (level-2) were used with the NDSI, NDSAI, and EMI indices by utilizing visible and infrared bands. Table 1 describes the Landsat data characteristics utilized in this study. The study also used geological maps 1:250,000 (Iraqi Geological survey and mining) in conjunction with topographic maps 1:100,000 (Iraqi Survey Authority).

3.2. Preprocessing

Landsat satellite images level-2 data were atmospherically corrected and surface reflectance was generated at the data center of USGS using Landsat Ecosystem Disturbance Adaptive Processing System LEDAPS (Version 3.4) for Landsat-5 and Landsat-7 (Landsat, 2019), and Landsat-8 Surface Reflectance Code LaSRC (Version 1.5) for Landsat-8 (USGS, 2018). These images are provided and available as ready products, which means these datasets series can be retrieved without any preprocessing from the end-users (Agapiou, 2020). More information about Landsat Level-2 can be found on the following website (https://www.usgs.gov/land-resources/nli/landsat/landsat-collection-2-level-2-science-products). ArcGIS 10.5 (Environmental Systems Research Institute, California, CA, USA), ENVI 5.3 (Exelis Visual Information Solutions, Boulder, CO, USA) and ERDAS 2015 (Hexagon Geospatial, 2015) software were used in the data processing. The first step was to combine Landsat bands using a layer stacking tool. Next step, the images were clipped using the perimeters of the study area.

4. Methodology

Two new indices for identifying and monitoring sandy areas are proposed in this study, namely NDSAI and SASTI, and then compared with other indices (NDSI and EMI) (Figure 3).

4.1. Normalized Differential Sand Areas Index (NDSAI)

A new Index (NDSAI) was developed by using the red and short-wavelength infrared SWIR1 bands as SWIR1 is more sensitive to the moisture content of soil than SWIR2 (Jasim AL-a'araage, 2012). Therefore, the areas of sand can be well distinguished from the rest of the soils and

Table 1. Characteristics of the Landsat images utilized in this study.

Satellites	Sensers	Data	Path/Row	Level	Spatial resolution
Landsat-5	TM	13-Aug-1987	167/37	Level-1 (Raw Data) and Level-2 (Surface Reflectance data products)	30m/Multispectral bands 60m/ Thermal bands
Landsat-7	ETM	29-July-2002	167/37		30m/Multispectral bands 15m/Panchromatic band 60m/ Thermal bands
Landsat-8	OLI	15-Aug-2017	167/37		30m/Multispectral bands 15m/Panchromatic band 100m/ Thermal bands

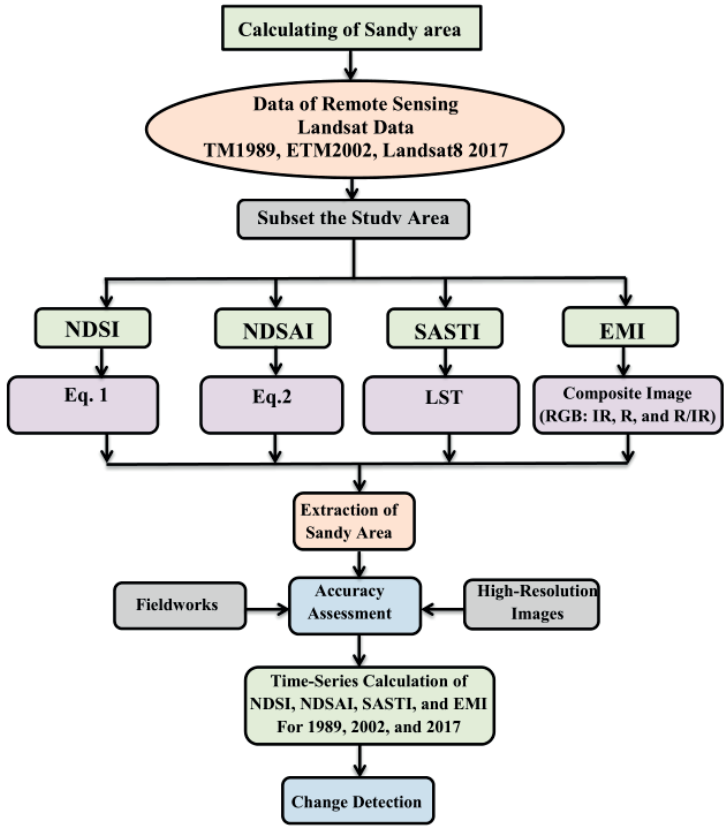

Figure 3. Flowchart showing the sandy indices adopted in the study.

vegetation areas since they are free of moisture in dry regions, or they rapidly lose water content in humid regions. The NDSAI formula is:

$$\mathrm{NDSAI} = \frac{\mathrm{SWIR1} - \mathrm{R}}{\mathrm{SWIR1} + \mathrm{R}} \qquad (2)$$

Where R represents the reflectance of the red band (0.63–0.69 μm); SWIR1 represents the reflectance of the short-wavelength infrared1 band (1.57–1.65 μm).

The values of NDSAI range between ($-1 \leq \mathrm{NDSAI} \leq 1$). The sandy areas, different kinds of soil, and vegetation areas have values often higher than zero (>0). The water has values less than zero (<0). The red band has been used in the negative sign of Equation 2 so that the sandy areas have a positive value since their reflectivity in the SWIR1 band is higher than in the red band.

4.2. Sandy Areas Surface Temperature Index (SASTI)

The SASTI index was developed based on the assumption that the temperature of sand dunes or sandy soil surface is higher than the temperature of all the other cover types. The temperatures of sandy areas are increased more rapidly than strong stone because they are unconsolidated and consist of fine-grained sediment. The materials of fine-grained, subsequently, have lower thermal inertia than the coarser materials (Fenton and Mellon, 2006). The thermal inertia is a measure for the response of a material's thermal to the diurnal heating cycle (Christensen, 1983), and has a strong effect on the spatial distribution of the Earth's surface temperature (Frey and Kuenzer, 2015). Increasing coarser-grained materials (i.e., sand, gravel, boulders, and bedrock) and consolidated sediments lead to the successively weaker diurnal

extreme from higher heat retention and therefore exhibit progressively higher thermal inertia values (Fenton and Mellon, 2006). Moreover, the drought of the sandy areas and its inability to conserve water is one of the factors that heat the sandy area more quickly than other materials. This study also assumed that climatic conditions are similar in the area of interest in the summer season and the highest temperature of the sandy area in the day is at 12 and reaches its peak about 1 pm at the local time while the highest annual temperature is in August (Zhang et al., 2012). Accordingly, satellite images were selected on August, with the exception of the 2002 image (end of July), and all images were obtained at around 11 am at local time.

4.2.1. Converting thermal DN values to temperature

There are many approaches used to mapping surface temperature from thermal scanner data (Lillesand and Kiefer, 2000). The measured at-sensor radiations are usually stored in converted digital numbers using a quantitative measurement system for the convenience of data storage. The values of digital numbers have no physical importance or unit, consequently, they must be converted into radiation, then into the at-sensor (top of atmosphere) brightness temperature, and then to LST (Land Surface Temperature), (Ghulam and Hall, 2010). The LST was retrieved from the thermal-bands of Landsat-5, Landsat-7, and Landsat-8 with a spatial resolution of 120 m for TM sensor, 60 m for ETM+ sensor, and 100 m for OLI sensor, respectively.

The digital numbers were first transformed to spectral radiances (Lλ) utilizing the parameters of the header files which came with satellite images and based on USGS 2013 equation (Zanter, 2016):

$$L\lambda = ML \cdot Q_{cal} + AL \quad (3)$$

Where Lλ is spectral radiance in W/(μm×m²×sr); *ML* is band radiance multiplicative re-scaling factor (Radiance Multi-Band-x from the metadata file); *AL* is band radiance additive re-scaling factor (Radiance Add Band-x from the metadata file); Q_{cal} is the quantized calibrated pixel value in DN. The output data of radiance Lλ was converted to at-sensor (top-of-atmosphere) brightness temperature by using Equation 4 (USGS, 2016), which was afterward converted to land surface temperature in Celsius by adding the absolute zero (approximately −273.15°C) (Avdan and Jovanovska, 2016).

$$T = \frac{K2}{\ln\left(\frac{K1}{L\lambda} + 1\right)} \quad (4)$$

Where T is the LST in Kelvin; K1 and K2 are the thermal conversion constant of the Landsat thermal bands.

4.3. Accuracy assessment of the sandy indices

To assess the accuracy of the classified images based on the sandy indices (NDSI, NDSAI, EMI, and SASTI), different measures, including producer accuracy (PA, omission errors), user accuracy (UA, commission errors), overall accuracy (OA) were calculated based on confusion matrices with 452 randomly distributed reference points for Landsat image acquired on August 15, 2017 (Figure 4). The confusion matrices are shown in Table 2.

Table 2. A confusion matrix with a summary of its equations. Where: PA represents the Producer's accuracy; UA represents the User's accuracy; OA represents the Overall accuracy; AC represents the chance agreement; RT represents the Row Total, and CT represents the Column Total; TP represents True Positive (the correct number of extracted sandy pixels); FN represents False Negative (the undetected number of sandy pixels); FP represents False Positive (the incorrect number of extracted sandy pixels), and TN represents True Negative (the correct number of rejected non-sandy pixels).

		Reference Data			
Classified data		Sandy	Non-sandy	Total	User's accuracy UA
	Sandy	TP	FP	RT_1=TP+FP	UA_1=TP/ RT_1
	Non-sandy	FN	TN	RT_2=FN+TN	UA_2=TN/RT_2
	Total	CT_1=TP+FN	CT_2=FP+TN	T=TP+TN	Overall Accuracy OA=TP+TN/T
	Producer's accuracy PA	PA_1=TP/CT_1	PA_2=TN/ CT_1		

$$AC = ([CT_1/T] \cdot [RT_1/T]) + ([CT_2/T] \cdot [RT_2/T]) \quad (1)$$

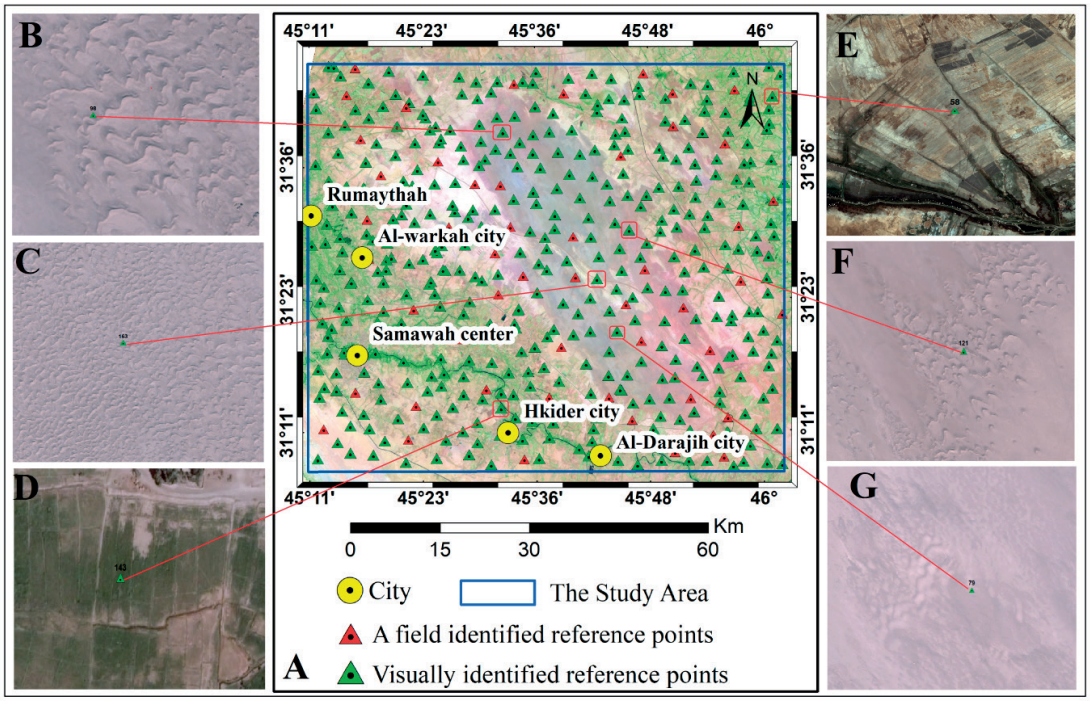

Figure 4. A QuickBird image with the random distribution of reference points, Figures B–G shows various examples of reference points for sandy and non-sandy areas extracted from high-resolution QuickBird images.

The first 400 points (about 88.4 % of all reference points) were selected randomly and then manually classified as either sandy area or non-sandy area with the support of the high-resolution images of Google Earth Pro™ acquired on December 2016, high-resolution imagery of ArcGIS server, and the pan-sharpened image (15 m) of Landsat-8. The remaining 52 (about 11.6 %) points were collected through fieldwork implemented during July 6 and 7, 2018. From the total of reference points, 153 (about 34 %) represent sandy areas, and 299 (about 66 %) represent non-sandy areas.

5. Results

5.1. Accuracy assessment

For accuracy assessment, binary classification was carried out with different thresholds for NDSAI and SASTI indices. These threshold values were selected based on the evaluation of classes and reference control points derived from high-resolution and medium-resolution images and field survey information (Figure 5). The NDSAI threshold utilized in this study was 0.05-0.12 for Landsat 8 and 0-0.1 for Landsat 7, while the threshold for the SASTI index was selected on the basis that sandy land temperature was about 4-5 °C higher than the other cover types. The error matrix and the results of the accuracy assessment used 452 reference points as shown in Table 3.

The NDSAI and SASTI indices are the best sandy indices to map most of the sandy surfaces, with UA about 85.8 % and 82 %, PA about 82 % and 79.6 %, and OA about 88.7 % and 86.5 %, respectively. The lower PA values than UA values are due to the mixing between the sandy and non-sandy pixels and to the moderate spatial resolution of Landsat imagery, therefore, the reflection value of the pixel will be closer to the area of the largest class within the same pixel. Therefore, some mixed pixels were classified as sandy, and others were classified as non-sandy areas. The commission errors of the NDSAI are due to misclassifying pixels that belonging to urban areas and mixed pixels, with very few pixels belonging to agricultural land.

Although the SASTI index can isolate many sandy and non-sandy pixels, it did not distinguish some sandy areas close to water or agricultural areas that contribute to a decrease in the temperature of the

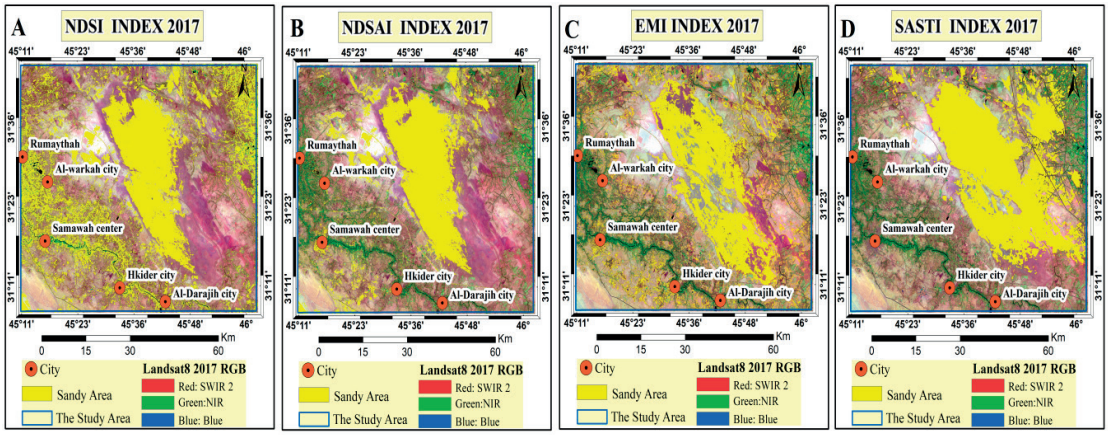

Figure 5. A, B, C, and D represented the binary classification for the NDSI and NDSAI, EMI, and SASTI respectively with different thresholds to separate the sandy areas from the non-sandy areas.

surrounding lands. Therefore, the accuracy of the SASTI index was not as accurate as the NDSAI as shown in Table 2. Generally, the performance of NDSAI and SASTI indices are better than other indices with OA of 89 % and 86 %, respectively.

The performance of the NDSI is poor when compared to the other indices because it fails to classify or isolate the vegetation area from the sandy area as shown in Figure 5.b and Figure 6 (the red squares). The lower UA about 74 % of the NDSI shows that omission error of sandy pixels is greater than commission error. Misclassification or isolation of vegetation cover sites is the main cause of increasing omission errors. PA of the EMI index is 64 % which is considered the worst. The low PA indicates that the index is unable to classify sandy surfaces correctly and thus contributes to a decrease in the overall accuracy that about 79 %.

5.2. Change detection

In this study, to obtain more information about sandy areas, change detection techniques were used by comparing the results of four indices

Table 3. Error matrix and accuracy assessment for different sandy indices.

NDSI				
		Reference Data		
		Sandy	Non-sandy	Total
Classified data	Sandy	128	44	172
	Non-sand	35	245	280
	Total	163	289	452

NDSAI				
		Reference Data		
		Sandy	Non-sandy	Total
Classified data	Sandy	133	22	155
	Non-sand	29	268	297
	Total	162	290	452

EMI				
		Reference Data		
		Sandy	Non-sandy	Total
Classified data	Sandy	99	40	139
	Non-sand	55	258	313
	Total	154	298	452

SASTI				
		Reference Data		
		Sandy	Non-sandy	Total
Classified data	Sandy	129	28	157
	Non-sand	33	262	295
	Total	162	290	452

Accuracy assessment for different sandy indices

Index	User's accuracy UA	Producer's accuracy PA	Overall Accuracy OA
NDSI	0.744	0.785	0.825
NDSAI	0.858	0.821	0.887
EMI	0.712	0.642	0.789
SASTI	0.821	0.796	0.865

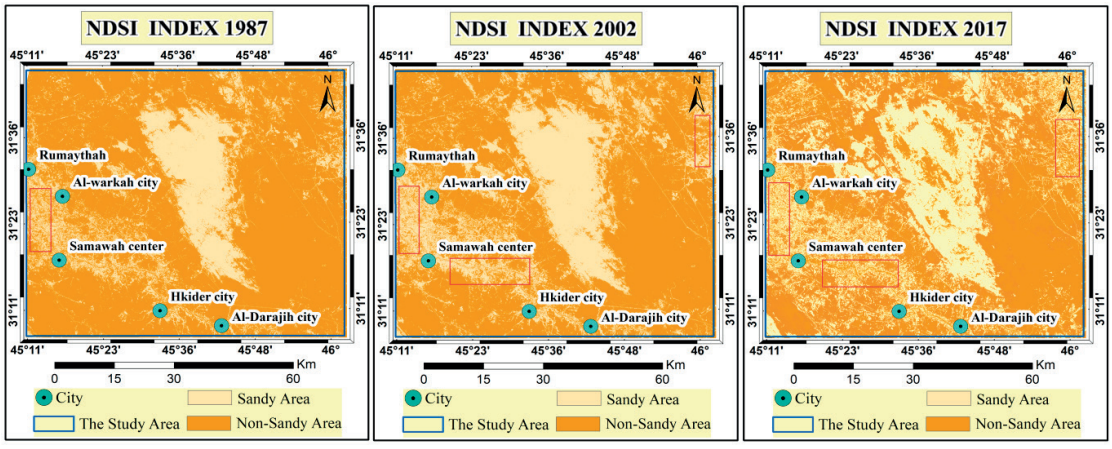

Figure 6. Sandy areas extracted by NDSI for the years 1987, 2002 and 2017.

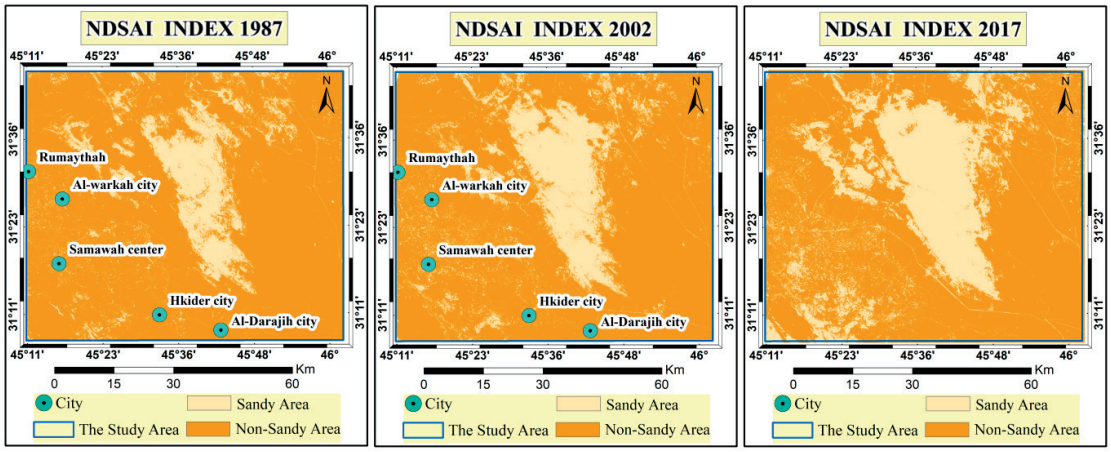

Figure 7. Sandy areas extracted by NDSAI for the years 1987, 2002 and 2017.

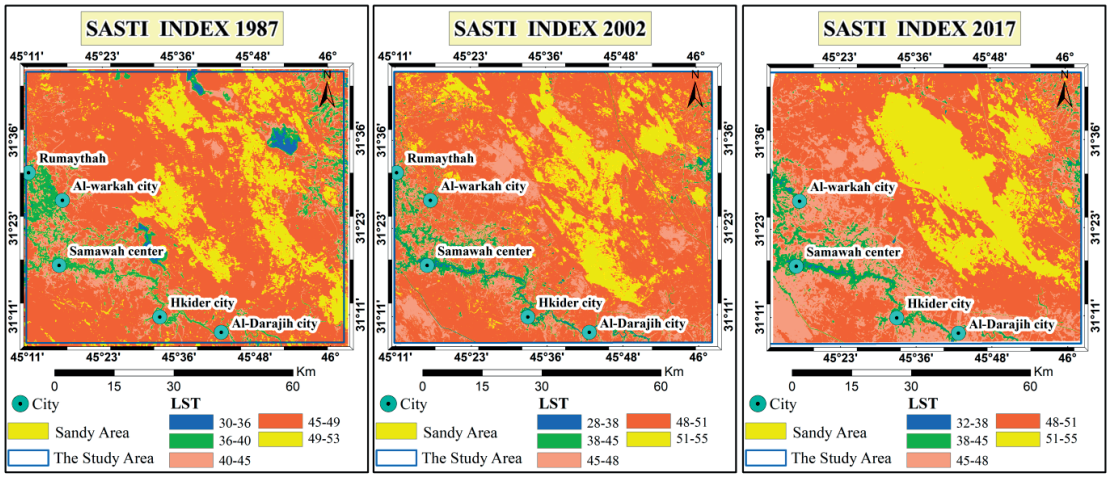

Figure 8. SASTI for the years 1987, 2002, and 2017, the sandy areas (yellow color) have the surface temperature is about 4-5°C higher than the temperature of other land covers. The water has the lowest surface temperature.

Table 4. Sand dunes cover area (in km^2) by use NDSI, NDSAI, EMI and SASTI.

Years	NDSI	NDSAI	EMI	SASTI
Area km^2 1987	1266	817	993	772
Area km^2 2002	1327	1012	1132	937
Area km^2 2017	1511	1147	1218	1125

for the period 1989-2017. The sandy areas were obtained from data of the related Landsat bands by using NDSI (Figure 6), NDSAI (Figure 7), and SASTI (Figure 8) for years 1987, 2002 and 2017. Table 3 shows the results of sandy indices calculation (in square kilometers). These results give us an idea about the spatial distribution of changes. There has been a marked increase in sandy areas over four decades from the period 1987 to 2002 and 2002 to 2017. The percentage of this increase was about 20% to 30% during 2002 and 2017 compared to 1989. All indices show that sandy areas accumulate mainly in the central part of the study area.

6. Discussion

Table 3 and Figures 6-8 show the area of sandy land as obtained from the NDSI, NDSAI, and SASTI. These results reveal that the values of sandy areas using NDSI have wide areas and differ significantly from the results of the other indices used. This is because the result included many agricultural areas and soil that could not be isolated by NDSI from the rest of the sandy lands (Figure 5.b and Figure 6, the red squares). Although SWIR2 band (2.08–2.35 μm) is sensitive to soil moisture (Acharya and Yang, 2015), it is more sensitive to the mineralogy of rocks and soils and has been frequently used by geologists to distinguish rock properties, geological formations, and faults since rocks and soils that appear similar in other ranges often have strong variations in SWIR domain (Loyd, 2013). But SWIR1 has more sensitivity to distinguish vegetation than SWIR2, since the energy incident upon vegetation is absorbed less in SWIR1, so the reflectivity in SWIR1 (at about 1.6 μm) is higher than in SWIR2 (at about 2.2 μm). This is the reason why the NDSI index was unable to isolate the sandy lands from the vegetation. So, the SWIR1 band was used to develop the new NDSAI.

The SWIR1 band has been used in the development of the Normalized Differential Moisture Index (NDMI) by (Wilson and Sader, 2002; Haubrock et al., 2008; Rokni et al., 2014) to characterize and analyze the moisture content. NDMI has been adopted by the US Geological Survey (https://www.usgs.gov/land-resources/nli/landsat/normalized-difference-moisture-index) and validated using laboratory reflectance measurements over many soil types (Fabre et al., 2015); hence combining SWIR1 with a red band in NDSAI, sandy areas were isolated easily from agricultural areas as well as other land covers due to their differences in terms of moisture content, under the assumption that sandy areas have less moisture content than other surfaces with low porosity, and they are composed of granules isolated from each other which contributed to the flow of water to the lower layers.

The spectral behavior of sand or sandy surfaces, in general, tend to increment reflection properties monotonically when increasing the wavelength, but soil moisture (water is considered a strong absorber in most wavelengths, especially in the infrared part of the spectrum), different mineral compositions of the surface and particle size are the main factors controlling surface reflection. The spectral reaction of different surfaces of soil relies upon many factors, specifically the physical condition (such as color, size, and moisture), mineralogical constituents and chemical composition. In addition, the shape of sand grains can have actual influence in the visible domain on the reflectance of sandy soils.

The main NDSAI limitation is the isolation of built from sandy areas. Vegetation areas can be masked by using different indices such as the Normalized Difference Vegetation Index NDVI that can improve the result as vegetation areas often reduce the reflectance values of the used bands reducing the overall accuracy. The

pixels cannot be removed or classified properly and this error will remain within the performance of all indices.

The temperature of the land surface of the study area was calculated using the thermal band (TIR) for Landsat images and it was concluded that the temperature of the sandy areas is greater than 4-5 °C with respect to the rest of covers. This difference in the land surface temperature of the sandy surface is produced considering several reasons, the most important ones are:

1. Sandy land is dry or low humidity compared to other types of covers.
2. The sand particles are not rigid or they do not contain links between them and thus they have the ability to gain heat from solar radiation with the first sunrise hours.
3. Sand is usually composed of solid metals such as quartz, a good heat transfer material.

The EMI was computed to identify the zone that is affected by wind erosion. The EMI is not helpful in extracting a sandy surface in an area with different cover types. The accuracy of the EMI may be increased if using the SWIR2 band instead of using the NIR band of Landsat imagery.

7. Conclusions

The importance of this work is that it provides quick methods that can be used in a short time and effort, and by utilizing a free moderated resolution satellite data to quickly detect and estimating the areas of sandy lands. Two new indices (NDSAI and SASTI) for sandy area estimation are proposed and presented in this study. These indices are compared with two indices (NDSI and EMI) that were previously proposed by other researchers. A confusion matrix has been applied to assess the accuracy and performance of these four indices.

The results concluded that RS data can be used as a strong tool in classifying and monitoring sandy areas. Visual inspection and validation data indicate the good performance of NDSAI index in classifying a wide variety of sandy areas based on the use of the SWIR1 band. This band generates more accurate results than SWIR2 band used in the NDSI index. SASTI index provides a performance close to the NDSAI index, and its results concluded that the temperature of sandy areas is 4-5° greater than in other types of covers. The performance of the NDSI index is poor because it fails to classify or isolate the vegetation area from the sandy area. Also, it might be better used in desert environments, or can be improved by masking the vegetation areas. The EMI performance is less robust than the other methods and it is not helpful in extracting a sandy surface in areas with different cover types. Further research in different regions around the world can contribute to detect the limitations of indices or enhancing their results.

References

Abbas, A. 2010. *Desertification Study of Dalmaj Lake Area in Mesopotamian Plain by Using Remote Sensing Techniques*. Baghdad University.

Abdul-Ameer, E.A. 2012. *The geomorphological study of dune fields and their environmental effects at Al-Muthana Governorate Iraq*. D. Sc. thesis, University of Baghdad, College of Science. 163p.

Acharya, T.D., Yang, I. 2015. Exploring landsat 8. *International Journal of IT, Engineering and Applied Sciences Research*, *4*(4), 4–10.

Agapiou, A. 2020. Evaluation of Landsat 8 OLI/TIRS Level-2 and Sentinel 2 Level-1C Fusion Techniques Intended for Image Segmentation of Archaeological Landscapes and Proxies. *Remote Sensing*, *12*(3), 579. https://doi.org/10.3390/rs12030579

Al-Khateeb A. 2007. *Climatic Changes and it's affect on geodynamic processes in Iraq during (1940–2000)*.

Avdan, U., Jovanovska, G. 2016. Algorithm for automated mapping of land surface temperature using LANDSAT 8 satellite data. *Journal of Sensors*, *2016*. https://doi.org/10.1155/2016/1480307

Azzaoui, M.A., Adnani, M., El Belrhiti, H., Chaouki, I.E., Masmoudi, L. 2019. Detection of crescent sand dunes contours in satellite images using an active shape model with a cascade classifier. *ISPAr*, *4212*, 17–24. https://doi.org/10.5194/isprs-archives-XLII-4-W12-17-2019

Bagnold, R.A. 2012. *The physics of blown sand and desert dunes*. Courier Corporation.

Baranoski, G.V.G., Kimmel, B.W., Chen, T.F., Miranda, E., Yim, D. 2013. Effects of sand grain shape on the spectral signature of sandy landscapes in the visible domain. *2013 IEEE International Geoscience and Remote Sensing Symposium-IGARSS*, 3060–3063. https://doi.org/10.1109/IGARSS.2013.6723472

Breed, C.S, Fryberger, S.G., Andrews, S., McCauley, C., Lennartz, F., Gebel, D., Horstman, K. 1979a. Regional studies of sand seas using Landsat (ERTS) imagery. In *A study of global sand seas* (Vol. 1052, pp. 305–397). US Geological Survey, Professional Paper.

Breed, C.S, Grolier, M.J., McCauley, J.F. 1979b. Morphology and distribution of common 'sand' dunes on Mars: Comparison with the Earth. *Journal of Geophysical Research: Solid Earth*, *84*(B14), 8183–8204. https://doi.org/10.1029/JB084iB14p08183

Brown, D.G., Arbogast, A.F. 1999. Digital photogrammetric change analysis as applied to active coastal dunes in Michigan. *Photogrammetric Engineering and Remote Sensing*, *65*, 467–474.

Buday, T. 1980. *The regional geology of Iraq: stratigraphy and paleogeography* (Vol. 1). State Organization.

Christensen, P.R. 1983. Eolian intracrater deposits on Mars: Physical properties and global distribution. *Icarus*, *56*(3), 496–518. https://doi.org/10.1016/0019-1035(83)90169-0

Fabre, S., Briottet, X., Lesaignoux, A. 2015. Estimation of soil moisture content from the spectral reflectance of bare soils in the 0.4–2.5 µm domain. *Sensors*, *15*(2), 3262–3281. https://doi.org/10.3390/s150203262

Fadhil, A.M. 2009. Land degradation detection using geo-informationtechnology for some sites in Iraq. *Journal of Al-Nahrain University-Science*, *12*(3), 94–108. https://doi.org/10.22401/JNUS.12.3.13

Fadhil, A.M. 2013. Sand dunes monitoring using remote sensing and GIS techniques for some sites in Iraq. *PIAGENG 2013: Intelligent Information, Control, and Communication Technology for Agricultural Engineering*, *8762*, 876206. https://doi.org/10.1117/12.2019735

Fenton, L.K., Mellon, M.T. 2006. Thermal properties of sand from Thermal Emission Spectrometer (TES) and Thermal Emission Imaging System (THEMIS): spatial variations within the Proctor Crater dune field on Mars. *Journal of Geophysical Research: Planets*, *111*(E6). https://doi.org/10.1029/2004JE002363

Frey, C.M., Kuenzer, C. 2015. Analysing a 13 years MODIS land surface temperature time series in the Mekong Basin. In *Remote Sensing Time Series* (pp. 119–140). Springer. https://doi.org/10.1007/978-3-319-15967-6_6

Gao, B.C. 1996. NDWI —A normalized difference water index for remote sensing of vegetation liquid water from space. *Remote Sensing of Environment*, *58*(3), 257–266. https://doi.org/10.1016/S0034-4257(96)00067-3

Hexagon Geospatial. 2015. *Erdas Imagine*. Hexagon AB: Stockholm, Switzerland.

Ghulam, A., Hall, M. 2010. *Calculating surface temperature using Landsat thermal imagery*. Department of Earth & Atmospheric Sciences, and Create for Environmental Sciences. Saint Louis University.

USGS. 2018. Landsat 8 surface reflectance code (LaSRC) product. Available at https://Landsat.Usgs.Gov/Sites/Default/Files/Documents/Lasrc_product_guide.Pdf (Accessed *on 26 December 2018)*.

Haubrock, S.N., Chabrillat, S., Kuhnert, M., Hostert, P., Kaufmann, H. 2008. Surface soil moisture quantification and validation based on hyperspectral data and field measurements. *Journal of applied remote sensing, 2*(1), 023552.

Hillel, D., Hatfield, J.L. 2005. *Encyclopedia of Soils in the Environment* (Vol. 3). Elsevier Amsterdam.

Hugenholtz, C.H., Levin, N., Barchyn, T.E., Baddock, M.C. 2012. Remote sensing and spatial analysis of aeolian sand dunes: A review and outlook. *Earth-Science Reviews*, *111*(3–4), 319–334. https://doi.org/10.1016/j.earscirev.2011.11.006

Jasim AL-a'araage, A.A. 2012. *Monitoring Desertification in Badra Area Eastern Iraq by Using Landsat Image Data*. Baghdad University.

Jassim, S.Z., Goff, J.C. 2006. *Geology of Iraq*. DOLIN, sro, distributed by Geological Society of London.

Khiry, M.A. 2007. Spectral mixture analysis for monitoring and mapping desertification processes in semi-arid areas in North Kordofan State, Sudan. *Published PhD Thesis, University of Dresden, Germany*.

Kourdian, R. 2009. *Analyse de la traficabilité en zone tropicale par imagerie spatiale optique et radar: application au Tchad méridional*. École Nationale Supérieure des Mines de Paris.

Landsat, U. 2019. Surface Reflectance Code (LASRC) Product Guide. *USGS and NASA: Reston, VA, USA*.

Lee, J.K., Acharya, T.D., Lee, D.H. 2018. Exploring land cover classification accuracy of Landsat 8 image using spectral index layer stacking in hilly region of South Korea. *Sensors and Materials*, *30*(12), 2927–2941. https://doi.org/10.18494/SAM.2018.1934

Levin, N., Ben-Dor, E. 2004. Monitoring sand dune stabilization along the coastal dunes of Ashdod-Nizanim, Israel, 1945–1999. *Journal of Arid Environments*, *58*(3), 335–355. https://doi.org/10.1016/j.jaridenv.2003.08.007

Lillesand, T.M., Kiefer, R.W. 2000. *Remote sensing and image interpretation*. John Wiley & Sons.

Loyd, C. 2013. *Landsat 8 Bands «Landsat Science*. https://landsat.gsfc.nasa.gov/landsat-8/landsat-8-bands/

McKee, E.D. 1979. Introduction to a study of global sand seas. In *A study of global sand seas* (Vol. 1052, pp. 1–19). Professional Paper. https://doi.org/10.3133/pp1052

Paisley, E.C.I., Lancaster, N., Gaddis, L.R., Greeley, R. 1991. Discrimination of active and inactive sand from remote sensing: Kelso Dunes, Mojave Desert, California. *Remote Sensing of Environment*, *37*(3), 153–166. https://doi.org/10.1016/0034-4257(91)90078-K

Pease, P.P., Bierly, G.D., Tchakerian, V.P., Tindale, N.W. 1999. Mineralogical characterization and transport pathways of dune sand using Landsat TM data, Wahiba Sand Sea, Sultanate of Oman. *Geomorphology*, *29*(3–4), 235–249. https://doi.org/10.1016/S0169-555X(99)00029-X

Pye, K., Tsoar, H. 2008. *Aeolian sand and sand dunes*. Springer Science & Business Media. https://doi.org/10.1007/978-3-540-85910-9

Ramsey, M.S., Christensen, P.R., Lancaster, N., Howard, D.A. 1999. Identification of sand sources and transport pathways at the Kelso Dunes, California, using thermal infrared remote sensing. *Geological Society of America Bulletin*, *111*(5), 646–662. https://doi.org/10.1130/0016-7606(1999)111%3C0646:IOSSAT%3E2.3.CO;2

Rokni, K., Ahmad, A., Selamat, A., Hazini, S. 2014. Water feature extraction and change detection using multitemporal Landsat imagery. *Remote Sensing*, *6*(5), 4173–4189. https://doi.org/10.3390/rs6054173

Rouse, J.W., Haas, R.H., Schell, J.A., Deering, D.W. 1974. Monitoring vegetation systems in the Great Plains with ERTS. *NASA Special Publication*, *351*, 309.

State Company for Geological Survey and mining. 2012. *Geological Map of Al-Nasiriya Quadrangle*.

Tsoar, H., Karnieli, A. 1996. What determines the spectral reflectance of the Negev-Sinai sand dunes. *International Journal of Remote Sensing*, *17*(3), 513–525. https://doi.org/10.1080/01431169608949024

USGS. 2016. Landsat Surface Reflectance Level-2 Science Products | Landsat Missions. https://landsat.usgs.gov/landsat-surface-reflectance-data-products

Walker, R.A. 2009. *The country in the city: the greening of the San Francisco Bay Area*. University of Washington Press.

Wasson, R.J., Hyde, R. 1983. Factors determining desert dune type. *Nature*, *304*5924, 337–339. https://doi.org/10.1038/304337a0

Wilson, E.H., Sader, S.A. 2002. Detection of forest harvest type using multiple dates of Landsat TM imagery. *Remote Sensing of Environment*, *80*(3), 385–396. https://doi.org/10.1016/S0034-4257(01)00318-2

Wolfe, S.A., Hugenholtz, C.H. 2009. Barchan dunes stabilized under recent climate warming on the northern Great Plains. *Geology*, *37*(11), 1039–1042. https://doi.org/10.1130/G30334A.1

Yamani M., Karami, F. 2011. Main Processes to Form and Move Morphology of Dunes in Khuzestan Plain (Case Study: Ahvaz North Sand). *Geographical Studies of Arid Places*, *2*.

Zanter, K. 2016. *Landsat 8 (L8) data users handbook*. Landsat Science Official Website.

Zha, Y., Gao, J., Ni, S. 2003. Use of normalized difference built-up index in automatically mapping urban areas from TM imagery. *International Journal of Remote Sensing*, *24*(3), 583–594. https://doi.org/10.1080/01431160304987

Zhang, Y.F., Wang, X.P., Pan, Y.X., Hu, R. 2012. Diurnal relationship between the surface albedo and surface temperature in revegetated desert ecosystems, Northwestern China. *Arid Land Research and Management*, *26*(1), 32–43. https://doi.org/10.1080/15324982.2011.631687